ACS APPLIED ENERGY MATERIALS

Cite This: ACS Appl. Energy Mater. 2019, 2, 1494−1504

Article

www.acsaem.org

Predictive Modeling of $CuInSe_2$ Nanocrystal Photovoltaics: The Importance of Band Alignment and Carrier Diffusion

Daniel W. Houck, Timothy D. Siegler, and Brian A. Korgel*

McKetta Department of Chemical Engineering and Texas Materials Institute, The University of Texas at Austin, Austin, Texas 78712, United States

Supporting Information

ABSTRACT: Nanocrystal inks have been used to make printed photovoltaic devices (PVs) with reasonably high efficiencies; however, little is actually known about the material properties that limit the performance of these devices. Here, we model the output characteristics of PVs with $CuInSe_2$ nanocrystal absorber layers using the Solar Cell Capacitance Simulator (SCAPS) software package and obtain the thickness-limited response and typical current−voltage behavior, power conversion efficiency (PCE), and external quantum efficiency (EQE) of experimentally fabricated PVs. The device behavior is accurately modeled using a low carrier mobility of 5×10^{-4} cm^2 V^{-1} s^{-1} and measured optical properties for the $CuInSe_2$ nanocrystal films. The simulations reveal that a reduction in the energy barrier for hole transport at the back contact and increased mobility and lifetime of charge carriers in the $CuInSe_2$ nanocrystal layer could improve device performance. Furthermore, this system is qualitatively different than the well-studied PVs of PbS nanocrystals, as manipulating the $CuInSe_2$ nanocrystal electron affinity by ligand exchange actually leads to unfavorable band alignment across the device and does not improve device performance.

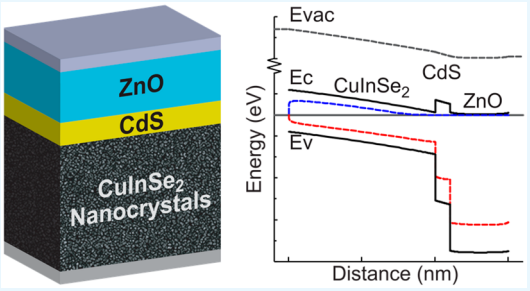

KEYWORDS: *nanocrystals, photovoltaics, copper indium selenide ($CuInSe_2$), solar cell device modeling, Solar Cell Capacitance Simulator (SCAPS), ligand exchange, nanocrystal photovoltaics*

INTRODUCTION

Photovoltaic devices (PVs) that use an absorber layer of $CuInSe_2$ nanocrystals can be made on a wide range of unusual substrate materials, including paper[1] and plastic.[2] These devices rely on the use of colloidal $CuInSe_2$ nanocrystals deposited from a solvent-based dispersion or ink without any further high temperature processing.[3,4] This creates new opportunities for integrated PV systems that cannot withstand harsh processing conditions.[5−8] To date, the power conversion efficiencies (PCEs) of $CuInSe_2$ nanocrystal PVs made without high temperature sintering of the nanocrystals by selenization have exhibited PCEs of about 3−4%.[4] This is significantly less than the efficiencies of the best vapor-deposited polycrystalline $Cu(In, Ga)Se_2$ (CIGS) layers fabricated at high temperature (>500 °C), which have exhibited efficiencies greater than 20%.[9−12] Solar Cell Capacitance Simulator (SCAPS) PV device modeling software, initially developed to model the device characteristics of CIGS solar cells,[13−28] has been used to model a variety of different PVs, ranging from flexible CdTe thin film devices to perovskites.[29−31] Here, we use SCAPS to model the performance characteristics of $CuInSe_2$ nanocrystal PVs fabricated without additional high temperature processing, identify the fundamental limitations of current devices, and reveal paths toward improvement.

The SCAPS simulations show that device efficiencies could be improved significantly—well above 10%—with a back contact with higher work function and increased carrier mobilities and lifetimes in the nanocrystal film. We were also interested in identifying fundamental differences between $CuInSe_2$ nanocrystal PVs and the PbS nanocrystal quantum dot PVs that have achieved a power conversion efficiency (PCE) exceeding 10% by tuning electron affinity with surface chemical treatments.[32] We found that ligand exchange strategies for tuning the electron affinity of $CuInSe_2$ nanocrystals will not lead to improved device performance.

EXPERIMENTAL AND MODELING

$CuInSe_2$ Nanocrystals. Indium(III) chloride ($InCl_3$, 99.99%), selenium powder (Se, 99.99%), oleylamine (OLAm, ≥98%), anhydrous toluene, tributylphosphine (TBP, 97%), and diphenylphosphine (DPP, 98%) were obtained from Sigma-Aldrich. Copper(I) chloride (CuCl, 99.999%) was obtained from Strem Chemicals. OLAm was degassed by maintaining a vacuum under 200 mTorr for 4 h at 110 °C and stored in a nitrogen filled glovebox. All other chemicals were used as received.

$CuInSe_2$ nanocrystals were synthesized according to published procedures.[1,33] In a nitrogen-filled glovebox, 5 mmol of CuCl, 5 mmol of $InCl_3$, 50 mL of OLAm, and 1.5 mL of DPP were added to a three-neck flask. The flask was removed from the glovebox and transferred to a Schlenk line. The flask was heated to 110 °C under a

Received: November 30, 2018
Accepted: January 11, 2019
Published: January 11, 2019

DOI: 10.1021/acsaem.8b02090
ACS Appl. Energy Mater. 2019, 2, 1494−1504

vacuum (200 mTorr) for 1 h. The flask was then filled with nitrogen and heated to 240 °C. In a separate vial in a glovebox, 10 mmol of Se powder was mixed with 10 mL of TBP. The TBP−Se mixture was injected into the reaction after reaching 180 °C. The temperature of the reaction flask was then maintained at 240 °C for 10 min and then removed from the heating mantle and allowed to cool to room temperature. $CuInSe_2$ nanocrystals were purified by antisolvent precipitation using ethanol.[1,33] The isolated nanocrystal product was redispersed in toluene at a concentration of 100 mg/mL. The reaction yields 740 mg of dispersible nanocrystals (44% molar conversion).

Transmission electron microscopy (TEM) images of nanocrystals drop-cast from toluene dispersions on carbon-coated nickel mesh TEM grids (Electron Microscopy Sciences) were acquired with a FEI Tecnai Spirit Bio Twin with 80 kV accelerating voltage. X-ray diffraction (XRD) of the nanocrystals was carried out using a Rigaku R-axis Spider Diffractometer with Cu Kα (λ = 1.54 Å) radiation with samples dried on a 0.5 mm nylon loop rotated at 1 deg/s and scanned for 10 min. Absorbance spectra were obtained for nanocrystals dispersed in toluene in a quartz cuvette with a concentration of 0.02 mg/mL using a Cary-5000 UV−vis-NIR spectrophotometer.

Absorption Coefficient Measurements. Absorption coefficient data for $CuInSe_2$ nanocrystals needed for the SCAPS simulation were experimentally measured. The transmittance and reflectance spectra were measured using a Carry 5000 UV-vis-NIR spectrophotometer with a diffuse reflectance accessory for nanocrystals spin-coated onto one square inch of polished soda-lime glass. The nanocrystals were deposited by spinning the substrate at 600 rpm for 3 s followed by 2000 rpm for 40 s. The absorption coefficient data between 850 and 880 nm were blanked from the data set input into the SCAPS simulation because of the noise in this wavelength region caused by the detector changeover. The thickness of the $CuInSe_2$ layer was estimated using a using a KLA Tencor D-500 profilometer. Thickness measurements were taken at three locations over the film, and each measurement varied by less than 20 nm from each other.

SCAPS Modeling. Table 1 lists the parameters used to simulate the response of $CuInSe_2$ nanocrystal PVs. These parameters were chosen on the basis of guidelines provided by Gloeckler et al.[34] for polycrystalline CIGS and the properties of $CuInSe_2$ nanocrystal absorber layers reported by Akhavan et al.[4] The key difference between the parameters used to simulate polycrystalline CIGS and $CuInSe_2$ nanocrystal devices is the charge carrier mobility in the absorber layer. As discussed below, the effective mobility of the electrons and holes that most accurately modeled the experimental device response was 5×10^{-4} cm^2 V^{-1} s^{-1}, which is 4 orders of magnitude lower than values measured for polycrystalline CIGS.[35,36] This value is in the range of effective charge carrier mobilities commonly observed in ligand capped metal chalcogenide nanocrystal films.[37−41]

Neutral, midgap, defects were included to simulate Shockley−Read−Hall (SRH) recombination, which tends to be the dominant recombination mechanism for photoexcited carriers in polycrystalline CIGS films.[34] The SRH lifetime τ is related to the thermal velocity ν, the defect concentration N, and the capture cross section of the defect $S_{capture}$:[34,42]

$$\tau = \frac{1}{\nu N S_{capture}} \quad (1)$$

The minority carrier SRH lifetime in the $CuInSe_2$ nanocrystal layer of a typical device calculated from the parameters given in Table 1 is 10 ns, which is consistent with the measured recombination lifetime in polycrystalline CIGS, which is often reported to be on the order of 1−10 ns.[43−47]

The barrier heights at the metal contacts Φ_b are defined by the differences in Fermi energy of the metal and the semiconductor band edge appropriate for the majority carriers.[48] The majority carrier barriers at the back and front metal contacts are 0.4 and 0.05 eV, corresponding to metal work functions of 5.10 and 4.45 eV, respectively. In the absence of Fermi level pinning, these values correspond to the reported work functions of contact layers of gold[49,50] and tin doped indium oxide (ITO)[51] typically used in $CuInSe_2$ nanocrystal PVs.

Table 1. Parameters Used in the SCAPS Simulation of $CuInSe_2$ Nanocrystal PVs

	$CuInSe_2$	CdS	ZnO
thickness (nm)	100	10	40
band gap (eV)	1.0	2.4	3.3
electron affinity (eV)	4.5	4.2	4.4
dielectric permittivity	13.6	10.0	9.0
conduction band density of states (cm^{-3})	2.2×10^{18}	2.2×10^{18}	2.2×10^{18}
valence band density of states (cm^{-3})	1.8×10^{19}	1.8×10^{19}	1.8×10^{19}
electron and hole thermal velocity (cm s^{-1})	1×10^{7}	1×10^{7}	1×10^{7}
electron mobility (cm^2 V^{-1} s^{-1})	5×10^{-4}	100	100
hole mobility (cm^2 V^{-1} s^{-1})	5×10^{-4}	25	25
donor density (cm^{-3})	0	1×10^{17}	1×10^{18}
acceptor density (cm^{-3})	2×10^{16}	0	0
defect type	neutral	neutral	neutral
capture cross section of electrons (cm^2)	1×10^{-13}	1×10^{-17}	1×10^{-15}
capture cross section of holes (cm^2)	1×10^{-15}	1×10^{-12}	1×10^{-12}
total defect density (cm^{-3})	1×10^{14}	1×10^{18}	1×10^{17}
energetic distribution	single at E_i	single at E_i	single at E_i
		back contact	front contact
electron recombination velocity (cm s^{-1})		1×10^{7}	1×10^{7}
hole recombination velocity (cm s^{-1})		1×10^{7}	1×10^{7}
majority carrier barrier relative to E_f (eV)		0.4	0.05
reflectivity		0.8	0.05

RESULTS

Optical Properties of $CuInSe_2$ Nanocrystal Films. For the model calculations of device performance, the optical absorption coefficients α of the CdS and ZnO layers were taken from Adachi et al.[52] For the $CuInSe_2$ nanocrystal layer, α was measured experimentally for thin films deposited on glass using an integrating sphere. The absorption coefficient α was determined from the measured reflectance R, transmission T, and thickness x of the nanocrystal film: $\alpha = (1/x)\ln((1-R)/T)$.[48] The thickness of the nanocrystal film used to determine α was determined by profilometry. The profilometry data are shown in Figure 1d; the average film thickness was 315 ± 8 nm. Parts a and b of Figure 1 show TEM and XRD of the nanocrystals. The average diameter of the nanocrystals was 10.3 ± 2.3 nm, and the XRD data match chalcopyrite $CuInSe_2$.[53] (See the Supporting Information for a histrogram of the nanocrystal size distribution.) Figure 1c shows optical absorbance spectra of the nanocrystals dispersed in toluene. The absorption edge is close to the bulk band gap of $CuInSe_2$, which is consistent with the relatively large nanocrystal size and a lack of quantum confinement.[53,57] Figure 1f shows the value of α for the nanocrystals compared to bulk $CuInSe_2$. The wavelength-dependent absorption coefficient of the nanocrystal film is about half of the value for polycrystalline $CuInSe_2$.[54] The lower absorption coefficient may be due to the significant void volume between nanocrystals in the film. Defects in the nanocrystals may also be playing a role, as the optical properties of the $CuInSe_2$

DOI: 10.1021/acsaem.8b02090
ACS Appl. Energy Mater. 2019, 2, 1494−1504

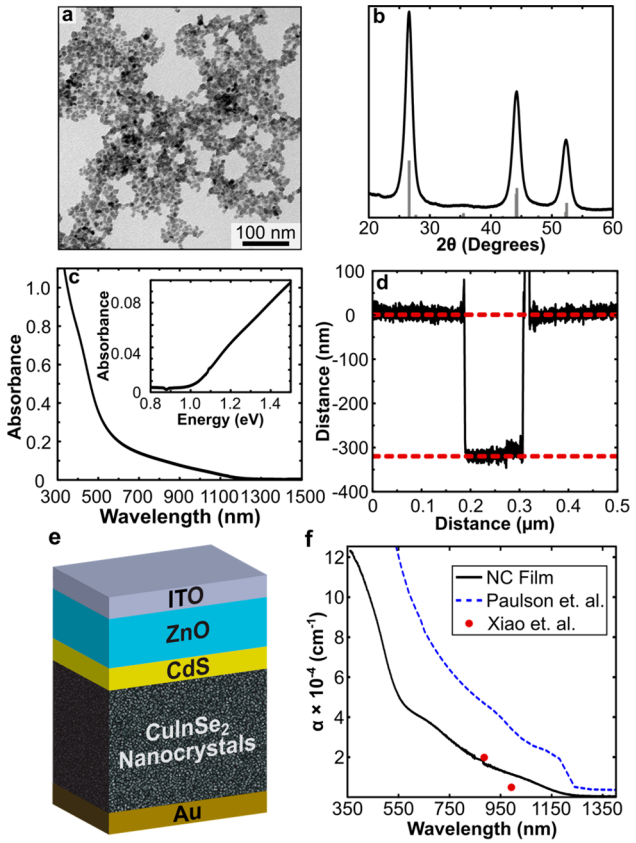

Figure 1. (a) TEM, (b) XRD, and (c) room temperature UV-vis-NIR absorbance spectra of the $CuInSe_2$ nanocrystals used to measure the optical absorption coefficient for input into the SCAPS device calculations. In part b, the gray drop lines correspond to JCPDS No. 00-040-1487 for chalcopyrite $CuInSe_2$. The spectra in part c were measured with the $CuInSe_2$ nanocrystals dispersed in toluene. The inset in part c shows the absorbance spectra rescaled to highlight the absorption onset energy. (d) Profilometry data used to estimate the $CuInSe_2$ nanocrystal film thickness. The dashed red lines are extrapolations of the data (black) at the substrate and surface of the nanocrystal layer. (e) Illustration of the materials stack for the $CuInSe_2$ PVs simulated in this work. (f) The absorption coefficient α, measured for a film of $CuInSe_2$ nanocrystals on glass that was used as input into the SCAPS device simulations. The absorption coefficient determined by Paulson et al.[54] for polycrystalline $CuInSe_2$ is shown by the dashed blue line, and absorption coefficients from Xiao et al.[55] for a $CuIn_3Se_5$ film are shown by red circles.

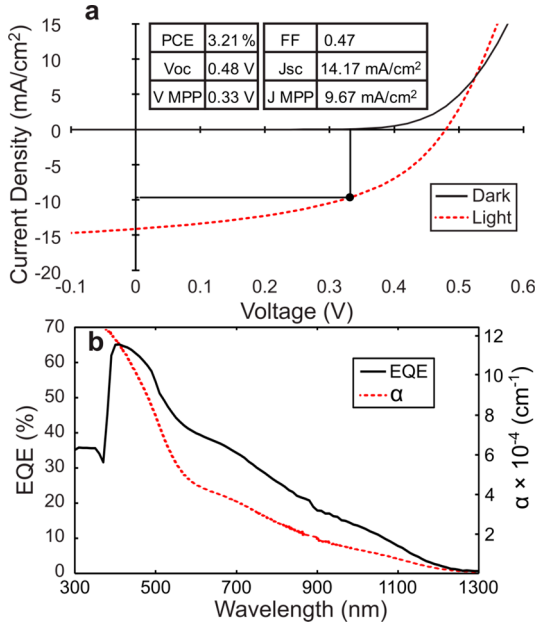

Figure 2. (a) $J-V$ curves and (b) EQE of a PV device with a 100 nm thick absorber layer of $CuInSe_2$ nanocrystals generated by SCAPS using the parameters in Table 1. The light $J-V$ curve is simulated using AM 1.5 conditions at 1000 W/m^2, and the EQE is simulated under short circuit conditions and 1000 W/m^2 AM 1.5 white light bias. The experimentally measured absorption coefficient data used for the SCAPS simulations are shown with the dashed red line.

nanocrystal film are much closer to the values of a Cu-deficient ordered vacancy compound (OVC), such as $CuIn_3Se_5$.[55] The $CuInSe_2$ nanocrystals are known to be deficient in copper; however, the band gap of 1.0 eV is similar to a polycrystalline $CuInSe_2$ film.[35,53,56] Figure 1e shows the device stack used in the simulations, and an electron affinity of 4.5 eV was used for the $CuInSe_2$ nanocrystals in the device simulations on the basis of reported values for polycrystalline $CuInSe_2$.[15,18,22]

The material parameters used in the SCAPS simulations are summarized in Table 1. Figure 2 shows the current–voltage characteristics ($J-V$ curve) and external quantum efficiency (EQE) response of a $CuInSe_2$ nanocrystal PV device simulated with a nanocrystal layer thickness of 100 nm. This thickness was used because it is similar to the nanocrystal thickness used in the report by Akhavan et al.[4] The experimentally observed PCE, V_{oc}, J_{sc}, and FF values of 3.21%, 0.48 V, 14.17 mA/cm^2, and 0.47 compare well to the calculated values of 3.10%, 0.41 V, 16.3 mA/cm^2, and 0.46. The "crossover" between light and dark $J-V$ curves in Figure 2a at 0.52 V results from changes in carrier concentration in the CdS layer under illumination and is commonly observed in $CuInSe_2$ and CIGS photovoltaics.[4,15,58] In the work of Akhavan et al.,[4] a crossover was observed at 0.41 V. The difference in the voltage at the crossover points is most likely due to differences in defect concentration in the CdS layer and interface that are not completely accounted for in the model. The EQE values in Figure 2b are relatively low between 1240 and 600 nm and increase significantly at shorter wavelengths between 375 and 600 nm. This is also consistent with experimental observations of Akhavan et al.,[4] resulting from the relatively thin nanocrystal layer and the noticeably distinct increase in α as the wavelength drops below ~600 nm. The drop in EQE at wavelengths less than 375 nm results from light absorption by the ZnO window layer.

Akhavan et al.[3,4] studied the effect of the $CuInSe_2$ nanocrystal layer thickness on device performance and found an optimum thickness of 150 nm for maximum PCE. This is too thin to absorb all of the incident light—conventional polycrystalline devices use CIGS layers that are several micrometers thick.[11,58] The device efficiency could be increased some by stacking devices using transparent top and bottom contacts, but the overall efficiencies of those devices were still limited.[3] Figure 3 shows device characteristics calculated using SCAPS for PVs with different nanocrystal layer thicknesses. The highest PCE was obtained in the simulations for devices with a nanocrystal layer of only 75 nm thick. This is thinner than what has been observed experimentally, most likely due to the fact that it is not practical to fabricate devices with spray-deposited nanocrystal

DOI: 10.1021/acsaem.8b02090
ACS Appl. Energy Mater. 2019, 2, 1494–1504

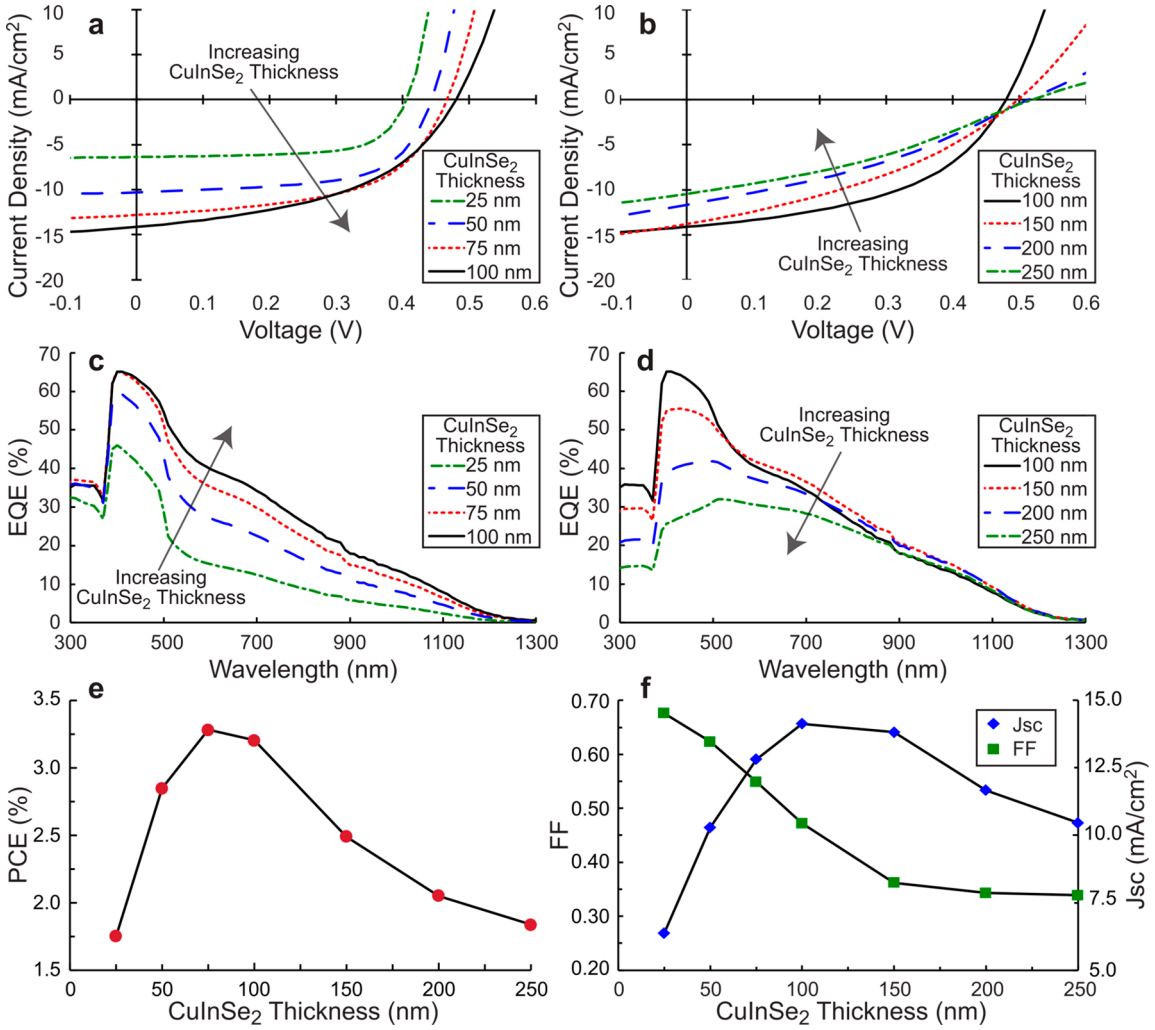

Figure 3. Simulated device response for $CuInSe_2$ nanocrystal PVs with different nanocrystal layer thicknesses. (a, b) $J-V$ curves for PV devices under 1000 W/m^2 AM 1.5 lighting with $CuInSe_2$ thicknesses ranging from 25 to 250 nm. (c, d) External quantum efficiency (EQE) for PV devices with $CuInSe_2$ thicknesses ranging from 25 to 250 nm under 1000 W/m^2 AM 1.5 white light bias and short circuit conditions. (e) Effect of $CuInSe_2$ nanocrystal layer thickness on PCE. (f) Effect of the $CuInSe_2$ nanocrystal layer thickness on FF and J_{sc}.

layers less than 100 nm thick, as the presence of even the slightest of pinholes leads to device shunting. In any case, the device simulations show that, although thicker nanocrystal layers absorb more light, the FF and the resulting PCE are decreased because the carrier mobility in the nanocrystal layer is so low. Devices with extremely thin $CuInSe_2$ layers have low J_{sc} because of insufficient light absorption, and low V_{oc} due to reduced quasi-Fermi level splitting resulting from the low free carrier concentration in the photoexcited film. When the nanocrystal film is thicker than 100 nm, the poor carrier mobility in the $CuInSe_2$ film begins to generate significant internal series resistance that results in the lowered FF observed in the $J-V$ curves in Figure 3b.[48]

One of the most appealing attributes of the nanocrystals is the ability to fabricate PVs at room temperature on a wide range of surfaces.[1−3] While polycrystalline CIGS layers are typically deposited on a Mo back contact, since Mo can withstand the high temperatures necessary to form CIGS,[58] $CuInSe_2$ nanocrystals can be deposited onto virtually any back contact.[1−3] The voltage output of the device depends on the energy barrier at the back contact,[48,59,60] and $CuInSe_2$ nanocrystal PVs have been fabricated on Au and Mo back contacts, with Au contacts providing a higher PCE.[3,4,61] The barrier heights in Table 1 used in the simulations assume no Fermi Level pinning and are based on Au and Mo work functions of 5.1 and 4.6 eV, respectively.[49,50] In a conventional polycrystalline CIGS device, a thin layer of $MoSe_2$ formed during the high temperature selenization process and Fermi level pinning effects significantly reduce the energy barrier at the back contact.[59,60] Figure 4a shows simulated $J-V$ curves for $CuInSe_2$ nanocrystal PVs with different barrier heights at the back contact. V_{oc} and PCE improve significantly as the barrier height is decreased, as summarized in Figure 4b. The maximum PCE of 5% obtained in the simulations occurs when the Fermi energy of the metal equals the quasi-Fermi level of the hole in the illuminated $CuInSe_2$ nanocrystal layer. Parts c−e of Figure 4 show the band alignment across the device layer under illumination. The device configuration exhibiting the maximum PCE has a barrier height at a back contact of 0.2 eV, at which point the Fermi level in the metal back contact aligns with the quasi-Fermi level for holes in the illuminated $CuInSe_2$ layer. These device simulations show that the PCE and V_{oc} of $CuInSe_2$ nanocrystal photovoltaics could

DOI: 10.1021/acsaem.8b02090
ACS Appl. Energy Mater. 2019, 2, 1494−1504

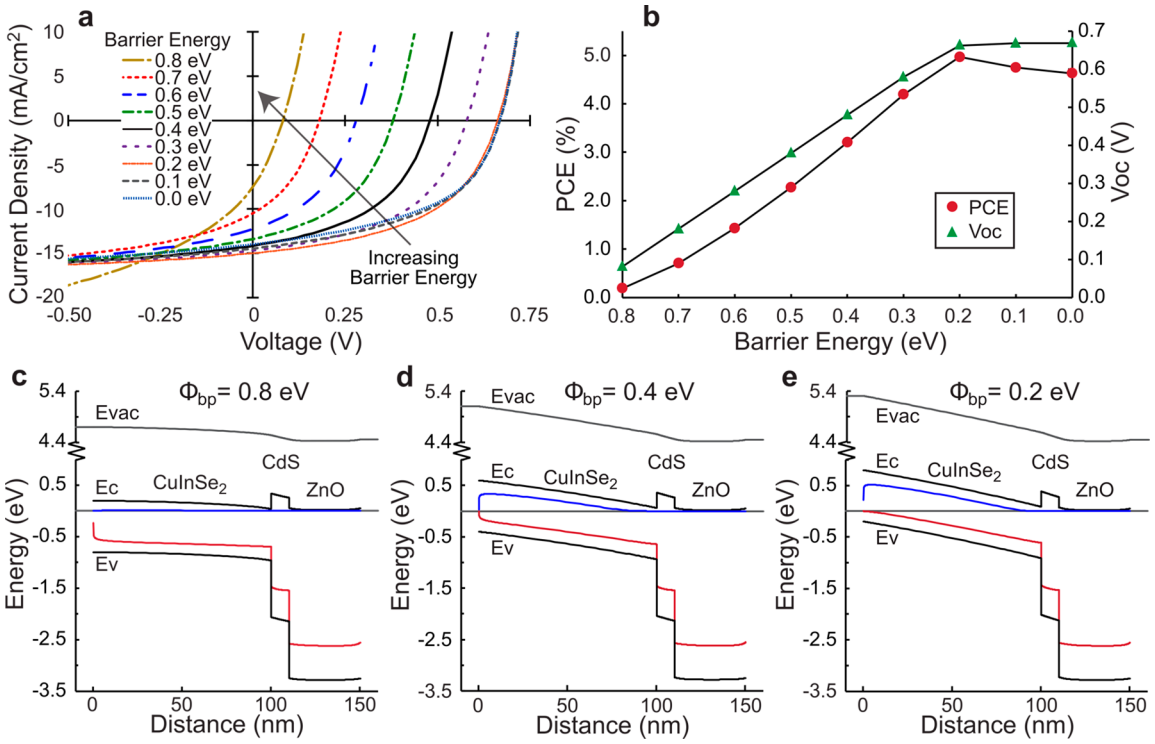

Figure 4. SCAPS simulations of $CuInSe_2$ nanocrystal PVs with various energy barriers at the back contact. The barrier energy (Φ_{bp}) is the energy difference between the Fermi level of the back contact and the $CuInSe_2$ valence band energy. (a) $J-V$ curves of PV devices under 1000 W/m^2 AM 1.5 lighting with Φ_{bp} varied between 0 and 0.8 eV. (b) Effect of Φ_{bp} on V_{oc} and PCE. (c–e) Energy band diagrams generated by SCAPS for PV devices under short circuit conditions with majority carrier barrier energies of 0.8, 0.4, and 0.2 eV, respectively. The quasi-Fermi levels of electrons and holes are indicated by the blue and red lines, respectively.

be improved with further optimization of the back contact and using a metal with a higher work function than gold.

Figure 5 shows the effect of improved electron and hole mobility in the $CuInSe_2$ nanocrystal layer on device performance. Perhaps counterintuitively, the device performance does not improve with increased carrier mobilities when the nanocrystal layer thickness remains constant. Figure 5 shows the response of a PV with a thin nanocrystal layer of 100 nm, similar to the condition that has yielded the highest efficiency experimentally. The increased mobility leads to an improved FF, but it reduces the V_{oc} and does not change J_{sc} significantly. The combination of these effects leads to little change in the PCE. J_{sc} does not change because it is already limited by the amount of light absorbed by the thin layer of nanocrystals, and V_{oc} decreases because the enhanced mobility reduces the concentration of photoexcited carriers in the absorber layer, which reduces the splitting of the quasi-Fermi levels. Increasing the mobility of the nanocrystal layer, however, would make it possible to use thicker nanocrystal layers to obtain higher performance, and ultimately provides a path toward higher efficiency devices. As shown in Figure 6, the nanocrystal layer thickness that yields optimum device performance increases significantly with improved carrier mobilities and PCE well above 10% is possible. As a benchmark, Figure 6b shows $J-V$ curves simulated for devices with carrier mobility μ, similar to polycrystalline CIGS (μ = 5 cm^2 V^{-1} s^{-1}). In this case, a nanocrystal layer thickness of 1 μm would yield a PCE of 12%.

In addition to the mobility, the carrier recombination lifetime also affects the charge carrier diffusion length and influences the performance of PV devices.[62] Figure 7 shows

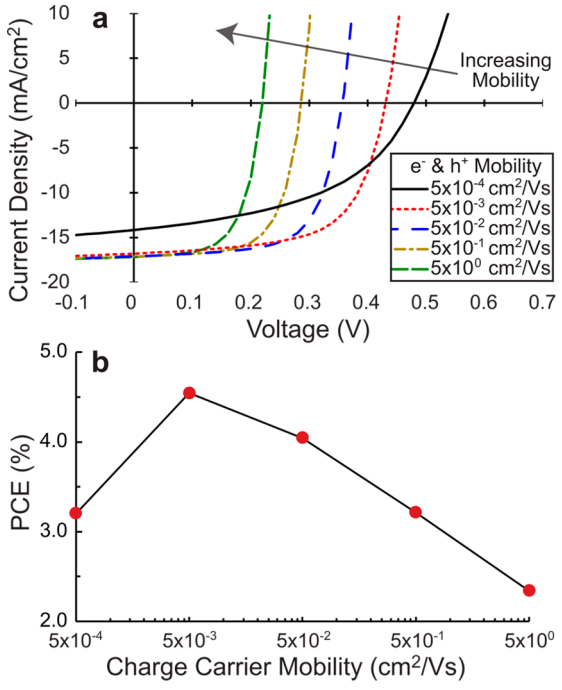

Figure 5. Simulated effect of the electron and hole mobility on the performance of a $CuInSe_2$ nanocrystal PV device with a constant $CuInSe_2$ layer thickness of 100 nm. The electron and hole mobilities were equal in each simulation. (a) $J-V$ curves and (b) PCE for PV devices under 1000 W/m^2 AM 1.5 illumination with the $CuInSe_2$ electron and hole mobilities varied from 5 × 10^{-4} to 5 cm^2 V^{-1} s^{-1}. The carrier lifetime was 10 ns.

DOI: 10.1021/acsaem.8b02090
ACS Appl. Energy Mater. 2019, 2, 1494–1504

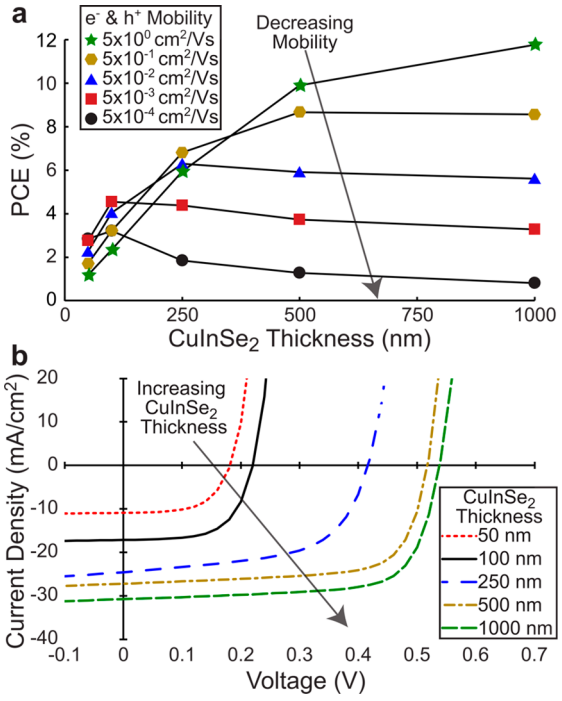

Figure 6. (a) Simulated effect of electron and hole mobility on the PCE of $CuInSe_2$ nanocrystal PV devices with $CuInSe_2$ layer thicknesses ranging from 50 to 1000 nm. The electron and hole mobilities were equal in each simulation. (b) $J-V$ curves for PV devices under 1000 W/m^2 AM 1.5 illumination with the $CuInSe_2$ layer thickness ranging from 50 nm to 1 μm and electron and hole mobilities of 5 cm^2 V^{-1} s^{-1}. The carrier lifetime was 10 ns.

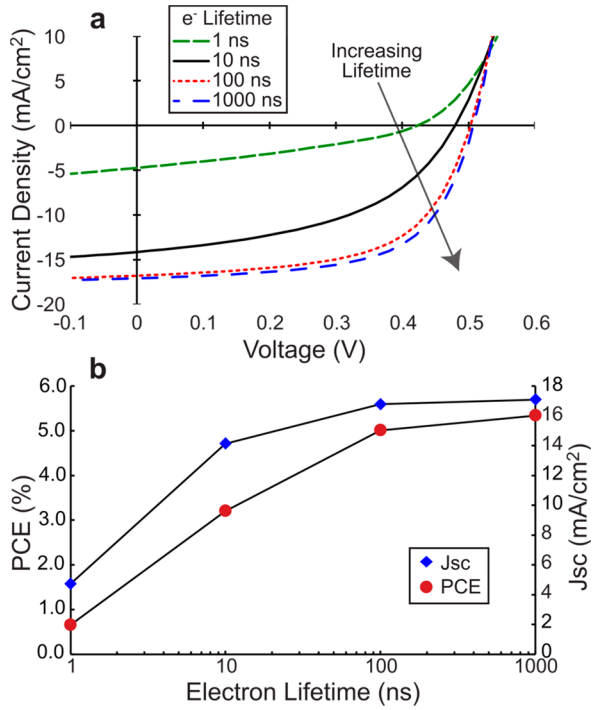

Figure 7. Simulated effect of carrier lifetime in the $CuInSe_2$ layer on the performance of a $CuInSe_2$ nanocrystal PV device with a constant $CuInSe_2$ layer thickness of 100 nm. The lifetimes τ were varied by changing the defect concentration N in the $CuInSe_2$ layer using eq 1 with cross sections for defect capture for electrons and holes of 1×10^{-13} and 1×10^{-15} cm^2. For comparison, the minority carrier lifetime of the $CuInSe_2$ device in Figure 2 is 10 ns. The capture cross section and thermal velocity for electrons and holes was the same for all device simulations. (a) $J-V$ curves for PV devices under 1000 W/m^2 AM 1.5 lighting where the minority carrier lifetime $CuInSe_2$ is varied from 1 to 1000 ns. (b) Effect of carrier lifetime in the $CuInSe_2$ layer on PCE and J_{sc}. The mobility was 5×10^{-4} cm^2 V^{-1} s^{-1}.

simulated device responses for PVs with thin 100 nm $CuInSe_2$ nanocrystal layers with various carrier lifetimes. Unlike the carrier mobility, increases in carrier lifetime could significantly improve the device efficiency without changing the nanocrystal film thickness. The experimentally observed PCE is about 3%, which corresponds to a carrier lifetime of about 10 ns, as shown in Figure 7b. Short lifetimes of 1 ns lead to devices with efficiencies lower than 1%. Short carrier lifetimes lead to low J_{sc} because of the loss of carriers due to the high rate of carrier recombination. The resulting loss in carrier concentration because of the significant recombination also lowers V_{oc} because of the corresponding lowering of the quasi-Fermi level splitting. An increase in carrier lifetime to 100 ns would bring the PCE to about 5%. Improvements in PCE are much less when the minority carrier lifetime increases above 100 ns because the PV performance again becomes limited by the amount of light absorbed by the thin (100 nm) nanocrystal layer. The maximum PCE for a device with such a thin nanocrystal layer is about 6%, with carrier lifetimes of >1 μs.

Figure 8 shows simulated device performance with varying carrier lifetimes when the $CuInSe_2$ nanocrystal layer thickness is modified. There is an optimum layer thickness for different carrier lifetimes. For example, when the lifetime is very short (1 ns), the highest performance is achieved for extremely thin nanocrystal layers. The highest efficiency shown in Figure 8a is 10%, corresponding to a layer thickness of 500 nm with a carrier lifetime of 1 μs. Even without any improvements in carrier mobility in the device layer, increases in the carrier lifetime could significantly improve device performance to >5%. The low mobility of the nanocrystal films ultimately limits the performance of the devices by creating internal series resistance that lowers J_{sc} and FF when the nanocrystal layer is too thick.

Another strategy for improving the efficiency of nanocrystal PVs has been to manipulate the electron affinity of the nanocrystals by surface modification of the capping ligands.[32,63] This has been done successfully in the case of PbS nanocrystal quantum dot PVs to achieve device efficiencies exceeding 10% without any high temperature processing.[32] Chuang et al.[32] suggest that ligand exchange chemistry on PbS nanocrystals can generate a relatively large electron affinity offset of 0.63 eV. This electron affinity offset was then used to create an electron blocking layer and extend the depletion region in the light absorbing layer. This approach was explored for $CuInSe_2$ nanocrystal PVs, as shown in Figures 9 and 10 (see also Tables S1–S4 in the Supporting Information). The SCAPS device simulations reveal that this is not a viable approach for $CuInSe_2$ nanocrystal devices. As shown in Figure 9a–d, there is a relatively narrow range of viable electron affinity values for optimal $CuInSe_2$ nanocrystal photovoltaics. Either an increase or decrease in the electron affinity of the nanocrystals results in reduced PCE. For lower electron affinity, this is the result of increased contact resistance that gives rise to rollover in the $J-V$ curves and low FF due to a poor conduction band offset between the $CuInSe_2$ and CdS, as shown in Figure 9e. When

DOI: 10.1021/acsaem.8b02090
ACS Appl. Energy Mater. 2019, 2, 1494–1504

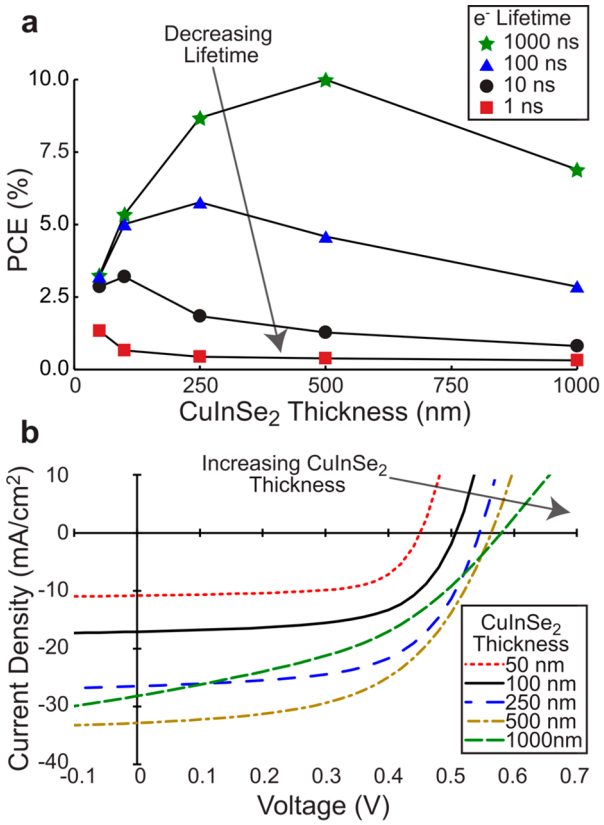

Figure 8. Effect of carrier lifetime in the $CuInSe_2$ layer on the performance of PV devices with varying $CuInSe_2$ nanocrystal layer thickness. Lifetimes were varied using the same approach as that described in the caption of Figure 7, using eq 1. (a) PCE of $CuInSe_2$ nanocrystal PV devices with the $CuInSe_2$ thickness varied from 50 nm to 1 μm and minority carrier lifetimes varied from 1 ns to 1 μs. (b) $J-V$ curves for PV devices under 1000 W/m^2 AM 1.5 lighting with various $CuInSe_2$ layer thicknesses and an electron lifetime of 1 μs. The mobility was 5×10^{-4} cm^2 V^{-1} s^{-1}.

the electron affinity is higher than 4.4 eV, the resistance at the back contact becomes a problem and leads to a drop in V_{oc} and PCE. Any alterations in the electron affinity of the $CuInSe_2$ nanocrystals will also require significant changes to the device architecture. Figure 10 shows the effects of graded or stepped electron affinity in the nanocrystal layer. As shown in Figure 10a, this leads to s-shaped $J-V$ characteristics. Essentially, the nanocrystal layer can be thought of as two $CuInSe_2$ layers with different maximum power point voltages. At the maximum power point voltage, the $CuInSe_2$ near the back contact is slightly overbiased, while the $CuInSe_2$ near the CdS is slightly underbiased. Several variations of this graded structure were studied, and none exhibited a major increase in device performance. The PCE, J_{sc}, V_{oc}, and FF for these devices are available in the Supporting Information.

DISCUSSION

Increasing the Carrier Mobility of $CuInSe_2$ Nanocrystal Films. Increasing the effective charge carrier mobility in the $CuInSe_2$ nanocrystal film so that it is closer to the mobility of polycrystalline CIGS is a conceptually straightforward strategy for improving the PCE; however, it has not yet been achieved in practice. For polycrystalline CIGS films, the majority and minority carrier mobilities have been measured by various techniques (such as the Hall effect,[64] photocarrier time-of-flight spectroscopy,[65] and high frequency admittance spectroscopy[66]) to be on the order of 1−10 cm^2 V^{-1} s^{-1}. The most common way to measure carrier mobility in nanocrystal films is to create a transistor and measure the field effect mobility.[38,40,41] Other techniques that have been used to characterize the mobility of nanocrystal films include time-of-flight spectroscopy[39] and time-resolved terahertz spectroscopy.[37] As deposited metal chalcogenide nanocrystal films with organic capping ligands tend to have mobilities on the order of 10^{-4} to 10^{-3} cm^2 V^{-1} s^{-1}, while various treatments can improve the mobility up to the order of 10^0 cm^2 V^{-1} s^{-1}.[37−41] A proven method used to improve the PCE of PbS nanocrystal PV devices is to implement surface ligand treatments to minimize the barrier between nanocrystals and increase the electron and hole mobility in the film.[67] The $CuInSe_2$ nanocrystal device simulation in Figure 3 uses electron and hole mobility values of 5×10^{-4} cm^2 V^{-1} s^{-1} for the untreated $CuInSe_2$ nanocrystal layer. The electron and hole mobilities were set equal in all simulations, which is a simplified first-order approximation; however, since the charge transport through a nanocrystalline film is typically dominated by nearest neighbor hopping, we expect the carrier mobilities to have similar, but not necessarily identical, values in any given film.[38] The SCAPS simulations show that higher carrier mobilities would lead to improved device performance. The ligand exchange strategies that have been used so successfully for PbS nanocrystals have not been readily applied to $CuInSe_2$ nanocrystals.[33,68] This could be because of chemical differences in the nature of the capping ligands and may require alternative approaches like a photonic curing[69] process that enables sintering nanocrystals without damaging the underlying substrate.

Increasing the Lifetime of Carriers in $CuInSe_2$ Nanocrystal Films. Carrier lifetime is generally measured in polycrystalline CIGS by time-resolved photoluminescence (TRPL), which probes photoluminescence intensity changes at ultrafast time scales.[43−47,70] These studies typically report recombination mechanisms dominated by the nonradiative Shockley−Read−Hall (SRH) process with lifetimes between 1 and 10 ns. However, by implementing strategies for defect passivation, much longer carrier lifetimes, dominated by radiative recombination processes, have been demonstrated. Metzger et al.[70] showed that eliminating oxidation of polycrystalline thin films can help extend the carrier lifetimes in polycrystalline CIGS thin films up to 250 ns, a value which was over an order of magnitude larger than previous reports. Additionally, Li et al.[71] demonstrated that $CuInS_2$ nanocrystals coated with a CdS or ZnS shell exhibit lifetimes near 500 ns, representing a three orders of magnitude enhancement compared to the bare nanocrystal cores. Our model indicates that increasing the carrier lifetime in the $CuInSe_2$ nanocrystal films using some variation of these methods can increase device efficiencies to nearly 10%.

CONCLUSIONS

Modeling the device response of $CuInSe_2$ nanocrystal PVs using SCAPS simulation software has provided insights about how to improve performance without resorting to high temperature processing of the nanocrystal layer. The simulated $J-V$ and EQE characteristics of the $CuInSe_2$ nanocrystal PVs show good agreement with experimental results and exhibit the expected thickness-limited performance. Reducing the majority carrier barrier at the back contact,

DOI: 10.1021/acsaem.8b02090
ACS Appl. Energy Mater. 2019, 2, 1494−1504

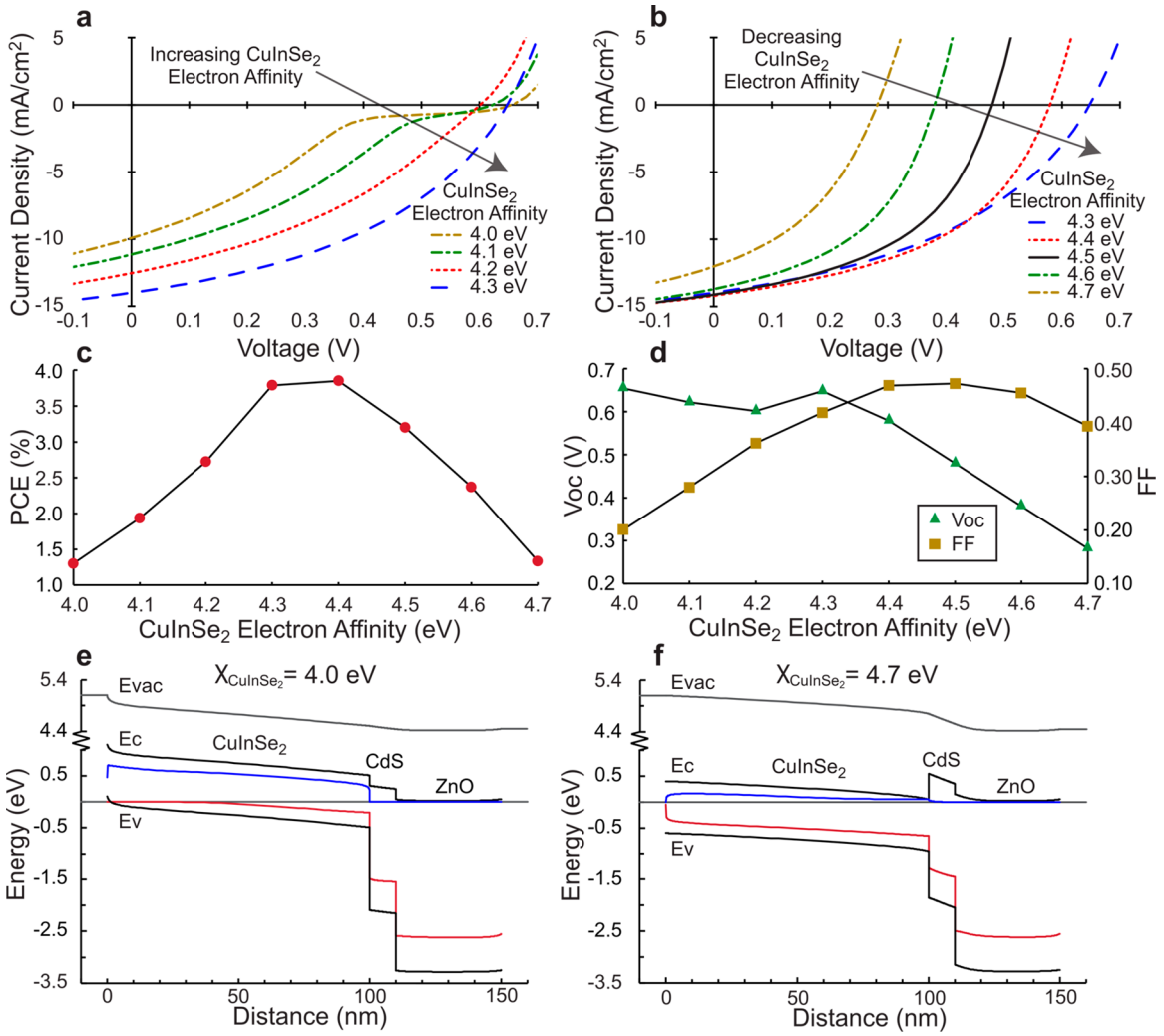

Figure 9. Simulated effect of the $CuInSe_2$ electron affinity on PV performance. (a, b) $J-V$ curves under 1000 W/m^2 AM 1.5 illumination with the $CuInSe_2$ election affinity varied from 4.0 to 4.7 eV. (c) Effect of the $CuInSe_2$ electron affinity on PCE. (d) Effect of the $CuInSe_2$ electron affinity on FF and V_{oc}. (e, f) Energy band diagrams generated by SCAPS for $CuInSe_2$ PV devices under short circuit conditions with electron affinities of 4.0 and 4.7 eV, respectively.

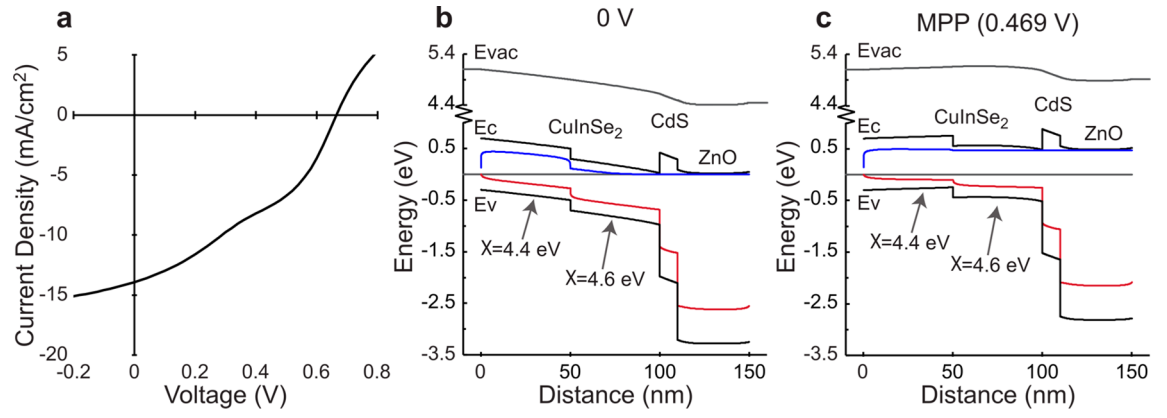

Figure 10. Performance of a PV device with a graded electron affinity in the $CuInSe_2$ nanocrystal layer. The electron affinity for the half of the layer near the back contact is 4.4 eV, and that for the half near the CdS layer is 4.6 eV. (a) $J-V$ curve for the device under 1000 W/m^2 AM 1.5 lighting. (b, c) Energy band diagrams generated by SCAPS for the device under (b) short circuit conditions and (c) the max power point voltage of 0.469 V.

increasing the effective charge carrier mobility in the $CuInSe_2$ film, and increasing the carrier lifetime $CuInSe_2$ film are all shown to be viable strategies for significantly improving device performance. Modifying the electron affinity of the $CuInSe_2$ layer, without making other significant changes to the device architecture, is shown to provide little to no improvement in

DOI: 10.1021/acsaem.8b02090
ACS Appl. Energy Mater. 2019, 2, 1494−1504

device efficiency. These results provide insight about how to improve material properties of ink-deposited $CuInSe_2$ nanocrystals in PV devices without resorting to high temperature processing.

■ ASSOCIATED CONTENT

Supporting Information

The Supporting Information is available free of charge on the ACS Publications website at DOI: 10.1021/acsaem.8b02090.

Histogram showing the nanocrystal size distribution and tabulated PCE, V_{oc}, J_{sc}, and FF for photovoltaic devices with variations of the graded electron affinity structure (PDF)

■ AUTHOR INFORMATION

Corresponding Author

*E-mail: korgel@che.utexas.edu. Phone: +1-512-471-5633.

ORCID

Brian A. Korgel: 0000-0001-6242-7526

Notes

The authors declare no competing financial interest.

■ ACKNOWLEDGMENTS

Funding of this research was provided by the Robert A. Welch Foundation (F-1464) and the National Science Foundation through the Industry/University Cooperative Research Center on Next Generation Photovoltaics (IIP-1540028 and IIP-1822206). T.D.S. acknowledges United States government support under and awarded by DoD, Air Force Office of Scientific Research, National Defense Science and Engineering Graduate (NDSEG) Fellowship, 32 CFR 168a. We would like to thank Marc Burgelman and The University of Gent for developing and providing access to the SCAPS simulation package.

■ REFERENCES

(1) Voggu, V. R.; Sham, J.; Pfeffer, S.; Pate, J.; Fillip, L.; Harvey, T. B.; Brown, R. M., Jr.; Korgel, B. A. Flexible $CuInSe_2$ Nanocrystal Solar Cells on Paper. *ACS Energy Lett.* **2017**, *2*, 574−581.

(2) Pernik, D. R.; Gutierrez, M.; Thomas, C.; Voggu, V. R.; Yu, Y.; van Embden, J.; Topping, A. J.; Jasieniak, J. J.; Vanden Bout, D. A.; Lewandowski, R.; Korgel, B. A. Plastic Microgroove Solar Cells Using $CuInSe_2$ Nanocrystals. *ACS Energy Lett.* **2016**, *1*, 1021−1027.

(3) Akhavan, V. A.; Goodfellow, B. W.; Panthani, M. G.; Reid, D. K.; Hellebusch, D. J.; Adachi, T.; Korgel, B. A. Spray-Deposited $CuInSe_2$ Nanocrystal Photovoltaics. *Energy Environ. Sci.* **2010**, *3*, 1600−1606.

(4) Akhavan, V. A.; Panthani, M. G.; Goodfellow, B. W.; Reid, D. K.; Korgel, B. A. Thickness-Limited Performance of $CuInSe_2$ Nanocrystal Photovoltaic Devices. *Opt. Express* **2010**, *18*, A411−A420.

(5) Zhan, Y.; Mei, Y.; Zheng, L. Materials Capability and Device Performance in Flexible Electronics for the Internet of Things. *J. Mater. Chem. C* **2014**, *2*, 1220−1232.

(6) Haight, R.; Haensch, W.; Friedman, D. Solar-Powering the Internet of Things. *Science* **2016**, *353*, 124−125.

(7) Todorov, T. K.; Singh, S.; Bishop, D. M.; Gunawan, O.; Lee, Y. S.; Gershon, T. S.; Brew, K. W.; Antunez, P. D.; Haight, R. Ultrathin High Band Gap Solar Cells with Improved Efficiencies from the World's Oldest Photovoltaic Material. *Nat. Commun.* **2017**, *8*, 682.

(8) Ahmad, S.; George, C.; Beesley, D. J.; Baumberg, J. J.; De Volder, M. Photo-Rechargeable Organo-Halide Perovskite Batteries. *Nano Lett.* **2018**, *18*, 1856−1862.

(9) Green, M. A.; Emery, K.; Hishikawa, Y.; Warta, W.; Dunlop, E. D. Solar Cell Efficiency Tables (Version 41). *Prog. Photovoltaics* **2013**, *21*, 1−11.

(10) Chirila, A.; Reinhard, P.; Pianezzi, F.; Bloesch, P.; Uhl, A. R.; Fella, C.; Kranz, L.; Keller, D.; Gretener, C.; Hagendorfer, H.; Jaeger, D.; Erni, R.; Nishiwaki, S.; Buecheler, S.; Tiwari, A. N. Potassium-Induced Surface Modification of $Cu(In,Ga)Se_2$ Thin Films for High-Efficiency Solar Cells. *Nat. Mater.* **2013**, *12*, 1107−1111.

(11) Feurer, T.; Reinhard, P.; Avancini, E.; Bissig, B.; Löckinger, J.; Fuchs, P.; Carron, R.; Weiss, T. P.; Perrenoud, J.; Stutterheim, S.; Buecheler, S.; Tiwari, A. N. Progress in Thin Film CIGS Photovoltaics - Research and Development, Manufacturing, and Applications. *Prog. Photovoltaics* **2017**, *25*, 645−667.

(12) Jackson, P.; Wuerz, R.; Hariskos, D.; Lotter, E.; Witte, W.; Powalla, M. Effects of Heavy Alkali Elements in $Cu(In,Ga)Se_2$ Solar Cells with Efficiencies up to 22.6%. *Phys. Status Solidi RRL* **2016**, *10*, 583−586.

(13) Burgelman, M.; Nollet, P.; Degrave, S. Modelling Polycrystalline Semiconductor Solar Cells. *Thin Solid Films* **2000**, *361−362*, 527−532.

(14) Burgelman, M.; Decock, K.; Khelifi, S.; Abass, A. Advanced Electrical Simulation of Thin Film Solar Cells. *Thin Solid Films* **2013**, *535*, 296−301.

(15) Niemegeers, A.; Burgelman, M.; Herberholz, R.; Rau, U.; Hariskos, D.; Schock, H.-W. Model for Electronic Transport in $Cu(In,Ga)Se_2$ Solar Cells. *Prog. Photovoltaics* **1998**, *6*, 407−421.

(16) Klenk, R. Characterization and Modelling of Chalcopyrite Solar Cells. *Thin Solid Films* **2001**, *387*, 135−140.

(17) Asaduzzaman, M.; Hasan, M.; Bahar, A. N. An Investigation into the Effects of Band Gap and Doping Concentration on $Cu(In,Ga)Se_2$ Solar Cell Efficiency. *SpringerPlus* **2016**, *5*, 578.

(18) Frisk, C.; Platzer-Björkman, C.; Olsson, J.; Szaniawski, P.; Wätjen, J. T.; Fjällström, V.; Salomé, P.; Edoff, M. Optimizing Ga-Profiles for Highly Efficient $Cu(In,Ga)Se_2$ Thin Film Solar Cells in Simple and Complex Defect Models. *J. Phys. D: Appl. Phys.* **2014**, *47*, 485104.

(19) Burgelman, M.; Marlein, J. Analysis of Graded Band Gap Solar Cells with SCAPS. In *23rd European Photovoltaic Solar Energy Conference*; Valencia, Spain, 2008; 2151−2155.

(20) Decock, K.; Lauwaert, J.; Burgelman, M. Characterization of Graded CIGS Solar Cells. *Energy Procedia* **2010**, *2*, 49−54.

(21) Gloeckler, M.; Sites, J. R. Efficiency Limitations for Wide-Band-Gap Chalcopyrite Solar Cells. *Thin Solid Films* **2005**, *480−481*, 241−245.

(22) Mostefaoui, M.; Mazari, H.; Khelifi, S.; Bouraiou, A.; Dabou, R. Simulation of High Efficiency CIGS Solar Cells with SCAPS-1D Software. *Energy Procedia* **2015**, *74*, 736−744.

(23) Minemoto, T.; Matsui, T.; Takakura, H.; Hamakawa, Y.; Negami, T.; Hashimoto, Y.; Uenoyama, T.; Kitagawa, M. Theoretical Analysis of the Effect of Conduction Band Offset of Window/CIS Layers on Performance of CIS Solar Cells Using Device Simulation. *Sol. Energy Mater. Sol. Cells* **2001**, *67*, 83−88.

(24) Hsu, W.; Sutter-Fella, C. M.; Hettick, M.; Cheng, L.; Chan, S.; Chen, Y.; Zeng, Y.; Zheng, M.; Wang, H.-P.; Chiang, C.-C.; Javey, A. Electron-Selective TiO_2 Contact for $Cu(In,Ga)Se_2$ Solar Cells. *Sci. Rep.* **2015**, *5*, 16028.

(25) Chelvanathan, P.; Hossain, M. I.; Amin, N. Performance Analysis of Copper−Indium−Gallium−Diselenide (CIGS) Solar Cells with Various Buffer Layers by SCAPS. *Curr. Appl. Phys.* **2010**, *10*, S387−S391.

(26) Igalson, M.; Zabierowski, P.; Prządo, D.; Urbaniak, A.; Edoff, M.; Shafarman, W. N. Understanding Defect-Related Issues Limiting Efficiency of CIGS Solar Cells. *Sol. Energy Mater. Sol. Cells* **2009**, *93*, 1290−1295.

(27) Pianezzi, F.; Reinhard, P.; Chirilă, A.; Bissig, B.; Nishiwaki, S.; Buecheler, S.; Tiwari, A. N. Unveiling the Effects of Post-Deposition Treatment with Different Alkaline Elements on the Electronic Properties of CIGS Thin Film Solar Cells. *Phys. Chem. Chem. Phys.* **2014**, *16*, 8843−8851.

(28) Vermang, B.; Fjällström, V.; Pettersson, J.; Salomé, P.; Edoff, M. Development of Rear Surface Passivated Cu(In,Ga)Se_2 Thin Film Solar Cells with Nano-Sized Local Rear Point Contacts. *Sol. Energy Mater. Sol. Cells* **2013**, *117*, 505−511.
(29) Mahabaduge, H. P.; Rance, W. L.; Burst, J. M.; Reese, M. O.; Meysing, D. M.; Wolden, C. A.; Li, J.; Beach, J. D.; Gessert, T. A.; Metzger, W. K.; Garner, S.; Barnes, T. M. High-Efficiency, Flexible CdTe Solar Cells on Ultra-Thin Glass Substrates. *Appl. Phys. Lett.* **2015**, *106*, 133501.
(30) Minemoto, T.; Murata, M. Device Modeling of Perovskite Solar Cells Based on Structural Similarity with Thin Film Inorganic Semiconductor Solar Cells. *J. Appl. Phys.* **2014**, *116*, No. 054505.
(31) Mailoa, J. P.; Bailie, C. D.; Johlin, E. C.; Hoke, E. T.; Akey, A. J.; Nguyen, W. H.; McGehee, M. D.; Buonassisi, T. A 2-Terminal Perovskite/Silicon Multijunction Solar Cell Enabled by a Silicon Tunnel Junction. *Appl. Phys. Lett.* **2015**, *106*, 121105.
(32) Chuang, C.-H. M.; Brown, P. R.; Bulović, V.; Bawendi, M. G. Improved Performance and Stability in Quantum Dot Solar Cells through Band Alignment Engineering. *Nat. Mater.* **2014**, *13*, 796−801.
(33) Houck, D. W.; Korgel, B. A. Facile Exchange of Tightly Bonded L-Type Oleylamine and Diphenylphosphine Ligands on Copper Indium Diselenide Nanocrystals Mediated by Molecular Iodine. *Chem. Mater.* **2018**, *30*, 8359−8367.
(34) Gloeckler, M.; Fahrenbruch, A. L.; Sites, J. R. Numerical Modeling of CIGS and CdTe Solar Cells: Setting the Baseline. In *Proc. 3rd World Conf. Photovolt. Energy Convers.* 2003, *1*, 491−494.
(35) Madelung, O. *Semiconductors: Data Handbook*; Springer: Berlin, Heidelberg, 2004.
(36) Repins, I. L.; Stanbery, B. J.; Young, D. L.; Li, S. S.; Metzger, W. K.; Perkins, C. L.; Shafarman, W. N.; Beck, M. E.; Chen, L.; Kapur, V. K.; Tarrant, D.; Gonzalez, M. D.; Jensen, D. G.; Anderson, T. J.; Wang, X.; Kerr, L. L.; Keyes, B.; Delahoy, A.; Von Roedern, B. Comparison of Device Performance and Measured Transport Parameters in Widely-Varying Cu(In,Ga)(Se,S) Solar Cells. *Prog. Photovoltaics* **2006**, *14*, 25−43.
(37) Guglietta, G. W.; Diroll, B. T.; Gaulding, E. A.; Fordham, J. L.; Li, S.; Murray, C. B.; Baxter, J. B. Lifetime, Mobility, and Diffusion of Photoexcited Carriers in Ligand-Exchanged Lead Selenide Nanocrystal Films Measured by Time-Resolved Terahertz Spectroscopy. *ACS Nano* **2015**, *9*, 1820−1828.
(38) Liu, Y.; Gibbs, M.; Puthussery, J.; Gaik, S.; Ihly, R.; Hillhouse, H. W.; Law, M. Dependence of Carrier Mobility on Nanocrystal Size and Ligand Length in PbSe Nanocrystal Solids. *Nano Lett.* **2010**, *10*, 1960−1969.
(39) Yazdani, N.; Bozyigit, D.; Yarema, O.; Yarema, M.; Wood, V. Hole Mobility in Nanocrystal Solids as a Function of Constituent Nanocrystal Size. *J. Phys. Chem. Lett.* **2014**, *5*, 3522−3527.
(40) Draguta, S.; McDaniel, H.; Klimov, V. I. Tuning Carrier Mobilities and Polarity of Charge Transport in Films of $CuInSe_xS_{2-x}$ Quantum Dots. *Adv. Mater.* **2015**, *27*, 1701−1705.
(41) Kang, M. S.; Lee, J.; Norris, D. J.; Frisbie, C. D. High Carrier Densities Achieved at Low Voltages in Ambipolar PbSe Nanocrystal Thin-Film Transistors. *Nano Lett.* **2009**, *9*, 3848−3852.
(42) Burgelman, M.; Decock, K.; Niemegeers, A.; Verschraegen, J.; Degrave, S. *SCAPS Manual*, version 29; University of Gent: 2016.
(43) Keyes, B. M.; Dippo, P.; Metzger, W. K.; AbuShama, J.; Noufi, R. Changes in the Dominant Recombination Mechanisms of Polycrystalline Cu(In,Ga)Se_2 Occurring during Growth. *J. Appl. Phys.* **2003**, *94*, 5584−5591.
(44) Puech, K.; Zott, S.; Leo, K.; Ruckh, M.; Schock, H.-W. Determination of Minority Carrier Lifetimes in $CuInSe_2$ Thin Films. *Appl. Phys. Lett.* **1996**, *69*, 3375−3377.
(45) Ohnesorge, B.; Weigand, R.; Bacher, G.; Forchel, A.; Riedl, W.; Karg, F. H. Minority-Carrier Lifetime and Efficiency of Cu(In,Ga)Se_2 Solar Cells. *Appl. Phys. Lett.* **1998**, *73*, 1224−1226.
(46) Shimakawa, S.; Kitani, K.; Hayashi, S.; Satoh, T.; Hashimoto, Y.; Takahashi, Y.; Negami, T. Characterization of Cu(In,Ga)Se_2 Thin Films by Time-Resolved Photoluminescence. *Phys. Status Solidi A* **2006**, *203*, 2630−2633.
(47) Probst, V.; Stetter, W.; Riedl, W.; Vogt, H.; Wendl, M.; Calwer, H.; Zweigart, S.; Ufert, K.-D.; Freienstein, B.; Cerva, H.; Karg, F. H. Rapid CIS-Process for High Efficiency PV-Modules: Development towards Large Area Processing. *Thin Solid Films* **2001**, *387*, 262−267.
(48) Nelson, J. *The Physics of Solar Cells*, 1st ed.; World Scientific Publishing Co Inc: 2003.
(49) Eastman, D. E. Photoelectric Work Functions of Transition, Rare-Earth, and Noble Metals. *Phys. Rev. B* **1970**, *2*, 1−2.
(50) Michaelson, H. B. The Work Function of the Elements and Its Periodicity. *J. Appl. Phys.* **1977**, *48*, 4729−4733.
(51) Park, Y.; Choong, V.; Gao, Y.; Hsieh, B. R.; Tang, C. W. Work Function of Indium Tin Oxide Transparent Conductor Measured by Photoelectron Spectroscopy. *Appl. Phys. Lett.* **1996**, *68*, 2699−2701.
(52) Adachi, S. *Optical Constants of Crystalline and Amorphous Semiconductors: Numerical Data and Graphical Information*; Springer Science & Business Media: 1999.
(53) Houck, D. W.; Assaf, E. I.; Shin, H.; Greene, R. M.; Pernik, D. R.; Korgel, B. A. Pervasive Cation Vacancies and Anti-Site Defects in Copper Indium Diselenide ($CuInSe_2$) Nanocrystals. *J. Phys. Chem. C*, submitted for publication, **2019**.
(54) Paulson, P. D.; Birkmire, R. W.; Shafarman, W. N. Optical Characterization of $CuIn_{1-x}Ga_xSe_2$ Alloy Thin Films by Spectroscopic Ellipsometry. *J. Appl. Phys.* **2003**, *94*, 879−888.
(55) Xiao, H. Z.; Yang, L. C.; Rockett, A. Structural, Optical, and Electrical Properties of Epitaxial Chalcopyrite $CuIn_3Se_5$ Films. *J. Appl. Phys.* **1994**, *76*, 1503−1510.
(56) Allen, P. M.; Bawendi, M. G. Ternary I-III-VI Quantum Dots Luminescent in the Red to Near-Infrared. *J. Am. Chem. Soc.* **2008**, *130*, 9240−9241.
(57) Panthani, M. G.; Stolle, C. J.; Reid, D. K.; Rhee, D. J.; Harvey, T. B.; Akhavan, V. A.; Yu, Y.; Korgel, B. A. $CuInSe_2$ Quantum Dot Solar Cells with High Open-Circuit Voltage. *J. Phys. Chem. Lett.* **2013**, *4* (12), 2030−2034.
(58) Stanbery, B. J. Copper Indium Selenides and Related Materials for Photovoltaic Devices. *Crit. Rev. Solid State Mater. Sci.* **2002**, *27*, 73−117.
(59) Dharmadasa, I. M.; Bunning, J. D.; Samantilleke, A. P.; Shen, T. Effects of Multi-Defects at Metal/Semiconductor Interfaces on Electrical Properties and Their Influence on Stability and Lifetime of Thin Film Solar Cells. *Sol. Energy Mater. Sol. Cells* **2005**, *86*, 373−384.
(60) Dharmadasa, I. M. Fermi Level Pinning and Effects on $CuInGaSe_2$ -Based Thin-Film Solar Cells. *Semicond. Sci. Technol.* **2009**, *24*, No. 055016.
(61) Akhavan, V. A.; Harvey, T. B.; Stolle, C. J.; Ostrowski, D. P.; Glaz, M. S.; Goodfellow, B. W.; Panthani, M. G.; Reid, D. K.; Vanden Bout, D. A.; Korgel, B. A. Influence of Composition on the Performance of Sintered Cu(In,Ga)Se_2 Nanocrystal Thin-Film Photovoltaic Devices. *ChemSusChem* **2013**, *6*, 481−486.
(62) Hodes, G.; Kamat, P. V. Understanding the Implication of Carrier Diffusion Length in Photovoltaic Cells. *J. Phys. Chem. Lett.* **2015**, *6*, 4090−4092.
(63) Brown, P. R.; Kim, D.; Lunt, R. R.; Zhao, N.; Bawendi, M. G.; Grossman, J. C.; Bulović, V. Energy Level Modification in Lead Sulfide Quantum Dot Thin Films through Ligand Exchange. *ACS Nano* **2014**, *8*, 5863−5872.
(64) Firoz Hasan, S. M.; Subhan, M. A.; Mannan, K. M. The Optical and Electrical Properties of Copper Indium Di-Selenide Thin Films. *Opt. Mater.* **2000**, *14*, 329−336.
(65) Dinca, S. A.; Schiff, E. A.; Shafarman, W. N.; Egaas, B.; Noufi, R.; Young, D. L. Electron Drift-Mobility Measurements in Polycrystalline $CuIn_{1-x}Ga_xSe_2$ Solar Cells. *Appl. Phys. Lett.* **2012**, *100*, 103901.
(66) Lee, J.; Cohen, J. D.; Shafarman, W. N. The Determination of Carrier Mobilities in CIGS Photovoltaic Devices Using High-

DOI: 10.1021/acsaem.8b02090
ACS Appl. Energy Mater. 2019, 2, 1494−1504

Frequency Admittance Measurements. *Thin Solid Films* **2005**, *480–481*, 336–340.
(67) Tang, J.; Kemp, K. W.; Hoogland, S.; Jeong, K. S.; Liu, H.; Levina, L.; Furukawa, M.; Wang, X.; Debnath, R.; Cha, D.; Chou, K. W.; Fischer, A.; Amassian, A.; Asbury, J. B.; Sargent, E. H. Colloidal-Quantum-Dot Photovoltaics Using Atomic-Ligand Passivation. *Nat. Mater.* **2011**, *10*, 765–771.
(68) Stolle, C. J.; Panthani, M. G.; Harvey, T. B.; Akhavan, V. A.; Korgel, B. A. Comparison of the Photovoltaic Response of Oleylamine and Inorganic Ligand-Capped $CuInSe_2$ Nanocrystals. *ACS Appl. Mater. Interfaces* **2012**, *4*, 2757–2761.
(69) Stolle, C. J.; Harvey, T. B.; Pernik, D. R.; Hibbert, J. I.; Du, J.; Rhee, D. J.; Akhavan, V. A.; Schaller, R. D.; Korgel, B. A. Multiexciton Solar Cells of $CuInSe_2$ Nanocrystals. *J. Phys. Chem. Lett.* **2014**, *5*, 304–309.
(70) Metzger, W. K.; Repins, I. L.; Contreras, M. A. Long Lifetimes in High-Efficiency $Cu(In,Ga)Se_2$ Solar Cells. *Appl. Phys. Lett.* **2008**, *93*, No. 022110.
(71) Li, L.; Pandey, A.; Werder, D. J.; Khanal, B. P.; Pietryga, J. M.; Klimov, V. I. Efficient Synthesis of Highly Luminescent Copper Indium Sulfide-Based Core/Shell Nanocrystals with Surprisingly Long-Lived Emission. *J. Am. Chem. Soc.* **2011**, *133*, 1176–1179.

DOI: 10.1021/acsaem.8b02090
ACS Appl. Energy Mater. 2019, 2, 1494–1504